

RESEARCH ARTICLE

10.1029/2020JF005640

Key Points:

- Combining Sentinel-1 SAR images and Sentinel-2 optical images to reconstruct 3D displacement field of a major landslide event
- Retrieving a 12-year landslide motion history using InSAR processing of ALOS and Sentinel images, and pixel offset tracking of LiDAR DEM gradients
- Developing a novel threefold rainfall threshold to forecast the dates for moderate/major movements of a deep-seated landslide

Supporting Information:

- Supporting Information S1

Correspondence to:

Y. Xu,
yuankunx@smu.edu

Citation:

Xu, Y., Lu, Z., Schulz, W. H., & Kim, J. (2020). Twelve-Year Dynamics and Rainfall Thresholds for Alternating Creep and Rapid Movement of the Hooskanaden Landslide From Integrating InSAR, Pixel Offset Tracking, and Borehole and Hydrological Measurements. *Journal of Geophysical Research: Earth Surface*, 125, e2020JF005640. <https://doi.org/10.1029/2020JF005640>

Received 6 APR 2020

Accepted 23 SEP 2020

Accepted article online 1 OCT 2020

Twelve-Year Dynamics and Rainfall Thresholds for Alternating Creep and Rapid Movement of the Hooskanaden Landslide From Integrating InSAR, Pixel Offset Tracking, and Borehole and Hydrological Measurements

Y. Xu¹ , Z. Lu¹ , W. H. Schulz² , and J. Kim¹ 

¹Roy M. Huffington Department of Earth Sciences, Southern Methodist University, Dallas, TX, USA, ²U.S. Geological Survey, Golden, CO, USA

Abstract The Hooskanaden landslide is a large (~600 m wide × 1,300 m long), deep (~30–45 m) slide located in southwestern Oregon. Since 1958, it has had five moderate/major movements that catastrophically damaged the intersecting U.S. Highway 101, along with persistent slow wet-season movements and a long-term accelerating trend due to coastal erosion. Multiple remote sensing approaches, borehole measurements, and hydrological observations have been integrated to interpret the motion behaviors of the slide. Pixel offset tracking of both Sentinel-1 and Sentinel-2 images was carried out to reconstruct the 3-D displacement field of the 2019 major event, and the results agree well with field measurements. A 12-year displacement history of the landslide from 2007 to 2019 has been retrieved by incorporating offsets from Light Detection and Ranging (LiDAR) digital elevation model (DEM) gradients and Interferometric Synthetic Aperture Radar (InSAR) processing of ALOS and Sentinel-1 images. Comparisons with daily/hourly ground precipitation reveal that the motion dynamics are predominantly controlled by intensity and temporal pattern of rainfall. A new empirical threefold rainfall threshold was therefore proposed to forecast the dates for the moderate/major movements. This threshold relies upon antecedent water-year and previous 3-day and daily precipitation and was able to represent observed movement periods well. Adaptation of our threshold methodology could prove useful for other large, deep landslides for which temporal forecasting has long been generally intractable. The averaged characteristic hydraulic conductivity and diffusivity were estimated as 6.6×10^{-6} m/s and 6.6×10^{-4} m²/s, respectively, based on the time lags between rainfall pulses and slide accelerations. Hydrologic modeling using these parameters helps to explain the ability of the new rainfall threshold.

1. Introduction

Landslides annually cause billions of dollars of property loss and thousands of casualties on a global scale (Froude & Petley, 2018; Spiker & Gori, 2003) and act as a primary instrument for geomorphic changes in many regions (Mackey & Roering, 2011; Simoni et al., 2013). Mitigating landslide hazards and understanding landslide-induced landscape evolution require knowledge of landslide kinematics and timing. However, the timing of deep-seated landslides is particularly problematic to forecast even with subsurface pore water pressure observations (Angeli et al., 1996; Gasparetto et al., 1996; Massey et al., 2013; Pyles et al., 1987; Schulz et al., 2009, 2018). Here we sought to use multiple remote sensing approaches and ground precipitation records to characterize motion behaviors of a typical deep-seated coastal landslide and to develop a rainfall thresholding strategy for forecasting the timing of its movements.

The Hooskanaden landslide, located in southwestern Oregon and crossed by U.S. Highway 101, has been constantly damaging the highway and has resulted in significant repair costs to the Oregon Department of Transportation (ODOT). The slide is large (~600 m wide × 1,300 m long), deep (~30–45 m), and has been active since at least 1958 (Parker, 1979) with typically slow motions in most years and occasional damaging moderate to major movements. Road maintenance during the slow-moving years annually cost ODOT about \$75,000, while repair costs of a single major event usually amount to \$5–7 million (ODOT, Oregon Department of Transportation, 2019). The most recent major event occurred on 25 February 2019, which

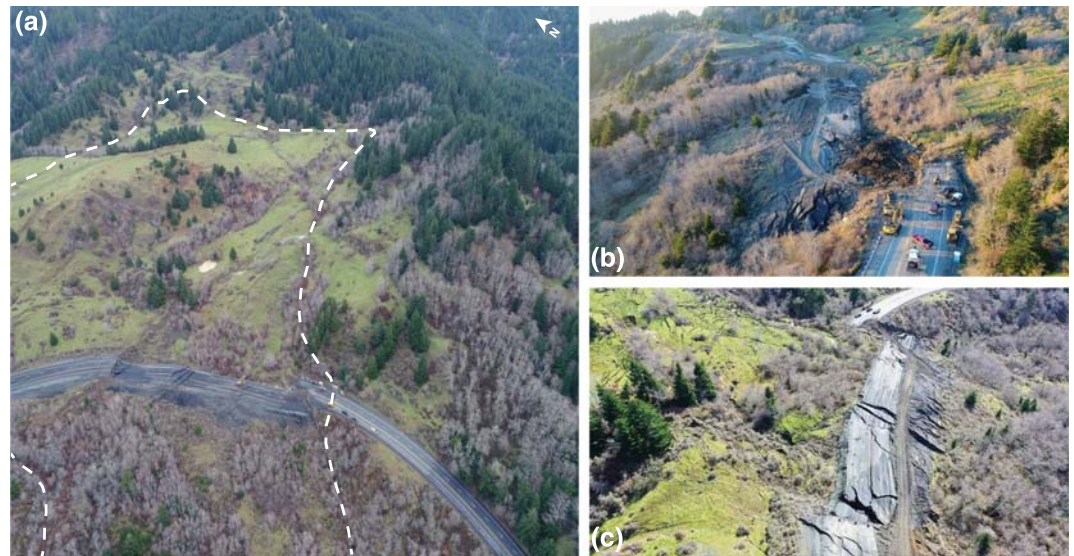


Figure 1. Photos of the 2019 February major slide. (a) Damaged roadway, and (b) a close-up, and (c) a side view of the damage from Tidewater Contractors, Inc. Note vehicles in each panel for scale. The white dashed line in (a) outlines boundaries of the 2019 February event based on field-surveyed fresh postevent cracks (Castro et al., 2019).

displaced the road surface about 40 m to the west and 17 m downward (Figure 1; Britton, 2019) and closed the highway for 13 days until a temporary gravel lane was opened (ODOT, Oregon Department of Transportation, 2019). Two paved lanes were later reconstructed and opened on 6 May, and a total of \$1.12 million had been spent by that time (ODOT, Oregon Department of Transportation, 2019). The Hooskanaden slide is a distinct example demonstrating that deep-seated landslides with long-term creeping behaviors may also move violently at certain times and cause significant damages.

To understand the motion behaviors of the Hooskanaden landslide, multiple remote sensing data sets and tools, borehole measurements, and hydrological observations were used for this investigation to retrieve its long-term surface and subsurface displacement history and reveal the role that precipitation plays. Specifically, InSAR (Interferometric Synthetic Aperture Radar) and pixel offset tracking of SAR images, optical images, and LiDAR (Light Detection and Ranging) DEMs (digital elevation models) were implemented to quantify the time series motion of the landslide from 2007 to 2019. The 2019 February event with significant block-like movements provided a special opportunity to reconstruct the three-dimensional (3D) surface deformation field by using pixel offset tracking of both the Sentinel-1 SAR images and the Sentinel-2 optical images. In addition, borehole inclinometer measurements were employed to reveal the landslide's subsurface motion dynamics and basal depths (Castro et al., 2019). Space-captured soil moisture from SMAP (Soil Moisture Active and Passive; Entekhabi et al., 2014) and ground precipitation measurements were used to quantify the hydraulic characteristics of the landslide and help investigate how rainfall impacts its motion dynamics.

This investigation demonstrates the ability of using multiple remote sensing approaches (InSAR, pixel offset tracking) and data sets (SAR, optical images, LiDAR DEMs) to reveal a landslide's movement time series and basal geometry (e.g., relative speeds and rotational failure mode) without application of any calibrated rheological models. These three-dimensional characterizations are of great importance for forecasting future landslide motions. Moreover, we successfully developed a threefold hydrological threshold to forecast the timing of the deep-seated landslide's seasonal onsets and moderate/major movements, by integrating shallow soil moisture from SMAP and daily/hourly ground precipitation. In contrast to the demanding and sometimes unreliable pore pressure thresholds (Angeli et al., 1996; Gasparetto et al., 1996; Massey et al., 2013), our hydrological thresholds do not require any expensive, potentially dangerous or impossible subsurface exploration and monitoring of pore water pressures and therefore can be easily adapted for other similar landslides.

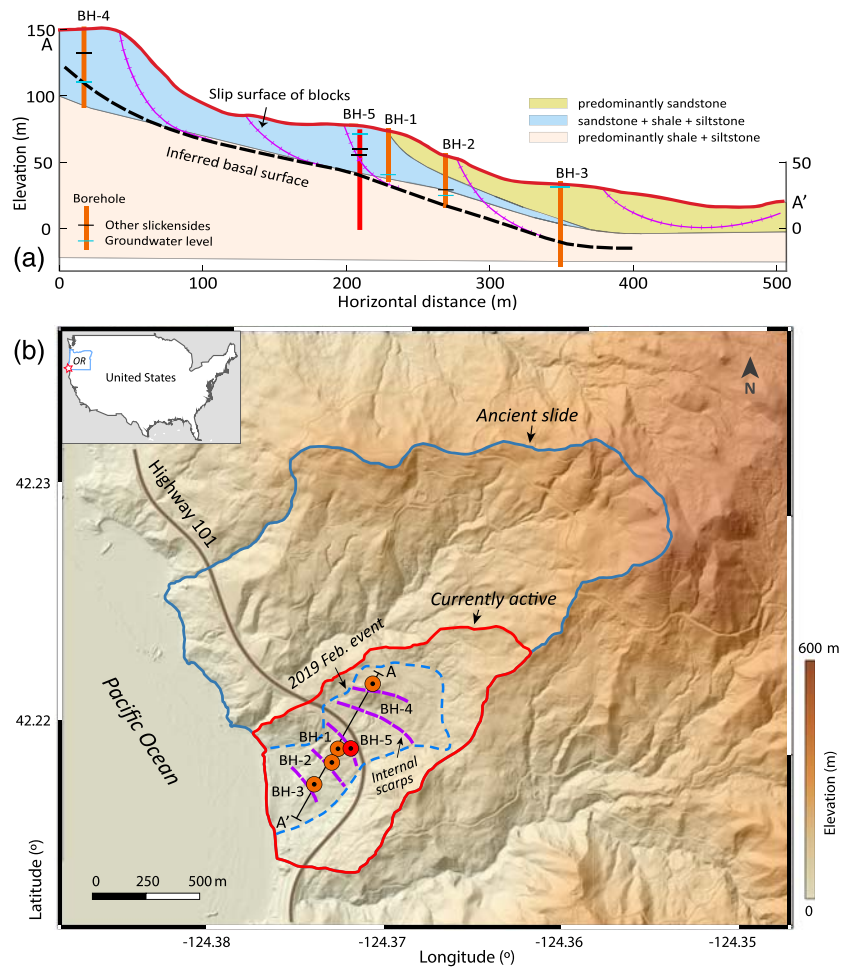


Figure 2. Geographical and geological settings of the Hooskanaden landslide. (a) A vertical cross section of the slide along A-A' shown in (b) and the stratigraphy inferred from five boreholes (BH-1 to BH-5). Boreholes 1–4 were drilled during 1978–1979, while BH-5 was drilled in 2017. (b) Geographical location of the landslide (red star mapped at the top left corner) and a shaded relief map generated from a 2008 LiDAR DEM. Boundaries of the February 2019 event are inferred from field-surveyed fresh postevent cracks (Castro et al., 2019).

2. Geological Setting and Historical Activities

2.1. Geographical and Geological Settings

The Hooskanaden landslide is located in Curry County, Oregon (Figure 2). The landslide is crossed near its center by U.S. Highway 101, and its toe reaches the Pacific Ocean (Figure 2b). The landslide crown is located at about 200 m in elevation, and the currently active body is about 1,300 m long and 600 m wide, with an average slope of 17°. Moderate surface vegetation consisting of grasses and deciduous and coniferous trees covers the lower half of the slide below the road, while sparse vegetation grows on the upper half (Figure 1a). The regional topography from the hillshade map (Figure 2b) indicates that the landslide at Hooskanaden may have experienced a large ancient event, along with subsequent fluvial erosion and mass wasting that have significantly modified the original landform.

Materials of the slide are derived from the Otter Point Formation of Late Jurassic geologic age (Walker & MacLeod, 1991), which consists of a matrix of sheared sandstone, mudstone, conglomerate, and interbedded sandstone and shale, with scattered BIMs (blocks-in-matrix, composed of more resistant sandstone, greenstones, chert, and blueschist). These materials, geologically referred to as *mélange* (Castro et al., 2019), accumulated as an accretionary wedge along the Cascadia subduction zone during tectonic displacement and formed the accreted western margin of the Klamath Mountains region (Orr & Orr, 2012). Stratigraphically,

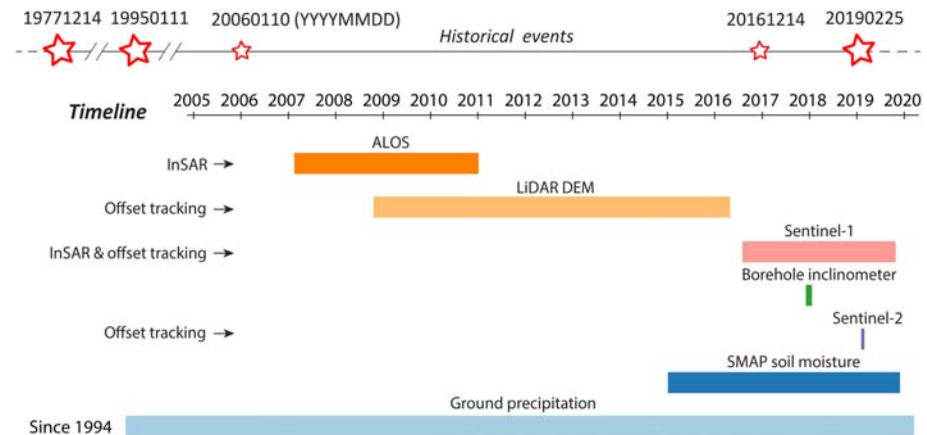


Figure 3. Historical moderate (smaller star) and major movements (bigger star), and time spans of remote sensing and ground-based data as shown by the timeline and corresponding data processing methods.

the slide consists of harder upper layers of predominantly sandstone and softer lower layers of mixed shale and siltstone, as indicated by samples collected from four boreholes drilled between September 1978 and January 1979 (Boreholes 1–4 in Figure 2a; Parker, 1979) and one borehole drilled in December 2017 (BH-5 in Figure 2a, ODOT drilling logs [Hole No. SPR808-H1]). Rocks in the borehole are either moderately weathered or highly fractured with numerous joints and slickensides. Depths of the main mass vary from 30 to 45 m (Parker, 1979).

Surface deformation patterns including localized slumps, compression ridges, transverse/semitransverse internal cracks and closed depressions (Figure 2b) indicate that the whole landslide comprises several compartmentalized zones of movement rather than a single mass moving as a coherent block. Individual compartment masses partly move along discrete basal shear zones but together contribute to the overall movement of the slide mass by alternatively providing and removing passive resistance and/or driving force to the compartments above and below. Lateral slide boundaries are potentially constrained by large BIMs present along the flanks of the landslide (Castro et al., 2019).

2.2. Historical Moderate and Major Slide Movements

The highway section near the Hooskanaden slide was opened in the early 1960s (Parker, 1979), and since 1958, three major events and two moderate ones noted by ODOT had reportedly displaced the highway by a significant amount (Figure 3; ODOT, Oregon Department of Transportation, 2019). The earliest major slide event was recorded on 14 December 1977, and the road surface dropped 2.5–3 m and slid 9 m to the west in the first 24 hr. The road was subsequently closed for 5 days. Seventeen years later on 11 January 1995, another major slide occurred, which shifted the roadway 4.3 m down and 12.2 m west in the first 24 hr and closed the highway for 8 days. After that, two moderate events were noted on 10 January 2006 and 14 December 2016, both dropping the road surface by 1.8 to 3 m. Most recently on 25 February 2019, another major movement was triggered and most of the movement occurred in the first few days. Movement in 2019 dropped the highway by 15–18 m in elevation and shifted the road 40 m to the west (Britton, 2019), and the road was consequently closed for about 2 weeks (ODOT, Oregon Department of Transportation, 2019). All the recorded moderate and major events were triggered in the wet winter rainy seasons from October through April.

3. Data and Methodology

3.1. Data

Multiple remote sensing and ground-measured data sets were used in this study. Remote sensing data including spaceborne SAR images from ALOS PALSAR (Advanced Land Observing Satellite; Phased Array type L-band Synthetic Aperture Radar) and Sentinel-1A/Sentinel-1B; airborne LiDAR DEMs, and Sentinel-2 optical images were employed for quantitative measurements of the slide motions (Figure 3). Twenty-one ALOS images from ascending track T224 between 2007 and 2011; three LiDAR DEMs

acquired in 2008, 2014, and 2016 (OLC, Oregon Lidar Consortium, 2020); and 84 Sentinel-1A/Sentinel-1B images from ascending track T35 between 2016 and 2019 were used altogether to retrieve the long-term displacement history of the Hooskanaden slide from February 2007 to November 2019. Two Sentinel-2 images acquired on January and March 2019, and 10 Sentinel-1A/Sentinel-1B images between January and March 2019 were used to reconstruct the three-dimensional displacement field of the February 2019 major movement. The 68-m-deep borehole inclinometer observations with 0.5-m vertical intervals between December 2017 and January 2018 were used to reveal the subsurface motion dynamics of the slide before the inclinometer was destroyed by slide movement (Castro et al., 2019). In addition, space-captured SMAP Level-4 soil moisture with 9×9 -km grid size from 2015 to 2019 (Entekhabi et al., 2014) and daily precipitation from a ground station located 12 km southwest of the slide from December 1994 to March 2020 (WRCC (Western Regional Climate Center), 2020) were used to provide hydrological observations.

3.2. InSAR

The InSAR method incorporates the phase information of SAR imagery to allow millimeter-scale displacement measurements along the LOS (line-of-sight) direction. We used this technique to quantify the long-term time series of slide displacement. The LiDAR DEM acquired in 2008 was used during interferogram generation using the GAMMA software (Werner et al., 2000), and the stratified tropospheric artifacts associated with surface topography were removed before phase unwrapping. Potential artifacts sourcing from regional soil moisture change and turbulent troposphere in each interferogram were removed by subtracting the InSAR phase of a common reference region (16×16 pixels after multilooking). This reference region is stable, very close to the landslide (within 1 km), and has constantly high coherence (greater than 0.7). The InSAR method was applied to the ALOS and Sentinel-1A/Sentinel-1B SAR data sets, and the multilooking factors were set as 3×7 (range by azimuth) and 5×2 , respectively. Accuracy of InSAR measurement can be quantified based on the coherence (Lu & Dzurisin, 2014; Rodriguez & Martin, 1992):

$$\sigma = \frac{\lambda}{4\pi} \sqrt{\frac{1}{2NM} \frac{(1-\gamma^2)}{\gamma^2}} \quad (1)$$

where σ is the uncertainty of InSAR measurements, λ the radar wavelength, N and M the window sizes for the coherence estimation, and γ the coherence. Time series measurements were achieved by using a coherence-weighted small baseline subset (SBAS) method (Tarantola, 2005; Tong & Schmidt, 2016). In matrix form, the time series inversion problem can be expressed as $\mathbf{G}\mathbf{m} = \mathbf{M}$, where \mathbf{G} is a matrix in the size of $[n \times s + 1]$ entailing InSAR observations and physical constraints, \mathbf{m} a matrix containing incremental displacements, \mathbf{M} the displacement observations of every interferogram, n the number of interferograms, and s the number of temporal increments. The equation can be expanded as follows:

$$\begin{bmatrix} 1 & 1 & 0 & \dots & \chi B_1 \\ 0 & 1 & 1 & \dots & \chi B_2 \\ \dots & \dots & \dots & \dots & \dots \\ \lambda/\Delta t_1 & -\lambda/\Delta t_1 & 0 & \dots & 0 \\ 0 & \lambda/\Delta t_2 & -\lambda/\Delta t_2 & \dots & 0 \end{bmatrix} \begin{bmatrix} m_1 \\ m_2 \\ \dots \\ m_s \\ \Delta h \end{bmatrix} = \begin{bmatrix} M_1 \\ M_2 \\ \dots \\ 0 \\ 0 \end{bmatrix} \quad (2)$$

where B_i and Δt_i are the perpendicular baseline and time interval of the i th interferogram, respectively; χ is a scaling factor determined by radar wavelength and the relative location between the satellite and ground targets. By introducing a weight matrix $\mathbf{P} = \text{diag} \{ \gamma_1, \gamma_2, \gamma_3, \dots, \gamma_n \}$, the incremental displacements can be solved as follows:

$$\mathbf{m} = (\mathbf{G}^T \mathbf{P} \mathbf{G})^{-1} \mathbf{G}^T \mathbf{P} \mathbf{M} \quad (3)$$

where \mathbf{G}^T denotes the transpose of \mathbf{G} . The covariance matrix of \mathbf{m} can be estimated as follows:

$$\mathbf{Q} = (\mathbf{G}^T \mathbf{P} \mathbf{G})^{-1} \hat{\sigma}^2 \quad (4)$$

where $\hat{\sigma}^2$ is the variance of the InSAR measurements. The small-baseline interferograms used for time series inversion were selected by setting a minimum coherence threshold of 0.4 for the L-band ALOS-1/ALOS-2

SAR images and 0.2 for the C-band Sentinel-1A/Sentinel-1B images before any filtering. A 32×32 moving window was used for coherence estimation, which corresponds to a minimum measurement uncertainty of ~ 1.4 mm for ALOS/ALOS-2 and ~ 0.7 mm for Sentinel-1A/Sentinel-1B interferograms.

3.3. Pixel Offset Tracking

Pixel offset tracking that uses normalized cross correlation (Bernstein & Colby, 1983; Scambos et al., 1992) to identify matched features and track offsets between features is another method to quantitatively measure landslide movements from remote sensing data. The achievable accuracy σ_{CR} of offset estimation via cross correlation is given as Equation 5 based on the Cramer-Rao bound (Bamler & Eineder, 2005):

$$\sigma_{CR} = \sqrt{\frac{3}{2NM}} \frac{\sqrt{1-\rho^2}}{\pi\rho} \cdot \sigma_{pix} \quad (5)$$

where N and M are window sizes for cross correlation, ρ is the cross-correlation coefficient, and σ_{pix} is the pixel resolution. A 32×32 window was used for cross correlation of all data (note that the window size must be two times greater than the to-be-measured displacement), and thresholds of cross-correlation coefficient were set to 0.2 for Sentinel-1 images, and 0.4 for Sentinel-2 and LiDAR data. Hence, the measurement accuracy ranges from 0.01 m for the 0.35-m-resolution LiDAR DEMs, to 0.28 m for the 10-m-resolution Sentinel-2 images and 0.8 m for the 14-m-resolution Sentinel-1 images in azimuth direction.

Offset tracking was applied to LiDAR DEMs, Sentinel-1A/Sentinel-1B SAR images, and Sentinel-2 optical images in this investigation. In contrast to the high-accuracy InSAR that uses phase information, pixel offset tracking of SAR data uses backscattered intensities and provides a rather lower accuracy. However, SAR offset tracking works better for measuring high-gradient displacement that could potentially cause decorrelation and phase unwrapping errors for InSAR. To enhance the performance of pixel offset tracking, varied preprocessing was implemented on Sentinel-1A/Sentinel-1B SAR data, Sentinel-2 optical images, and LiDAR DEMs.

3.3.1. Preprocessing of Sentinel-1/Sentinel-2 Images

We averaged multiple Sentinel-1A/Sentinel-1B SAR images to reduce the speckle noises and applied oversampling on the azimuth direction. The 10-m-resolution Sentinel-2 images were oversampled on both northing and easting directions, and both red and near-infrared bands of the multiband Sentinel-2 images were combined to enhance ground features by calculating SR (simple ratio):

$$SR = NIR/R \quad (6)$$

where NIR and R denote the near-infrared and red band, respectively. The simple ratio takes advantage of the relationship between high absorption by chlorophyll of red radiant energy and high reflectance of near-infrared energy for healthy leaves and plant canopies (Ollinger, 2011) and can therefore particularly highlight ground features composed of healthy vegetation and augment the performance of offset tracking.

Five Sentinel-1A/Sentinel-1B SAR images acquired before the event between 1 January and 18 February 2019 were averaged to form one SAR intensity image named 20190218.ave (Figure 4a), while another five acquired after the event between 14 March and 1 May 2019 were averaged to form an image named 20190314.ave (Figure 4b). Original 2.3-m \times 14-m (range by azimuth) pixel-sized Sentinel-1A/Sentinel-1B images were oversampled in the range direction to 2.3-m \times 2.8-m pixel size before offset tracking. Pixel offset tracking was implemented on the simple ratio (Equation 6) of Sentinel-2 images acquired on 31 January and 2 March 2019. An oversampling factor of 4 was applied to both northing and easting directions (Figures 4d and 4e).

3.3.2. Preprocessing of LiDAR DEMs

We applied pixel offset tracking of LiDAR DEMs on the elevation gradients instead of the elevations, because elevation gradient can better preserve topographical features than the elevation itself when vertical deformation exists. No oversampling was applied to the LiDAR DEM gradients before offset tracking. The elevation gradient G was calculated as follows:

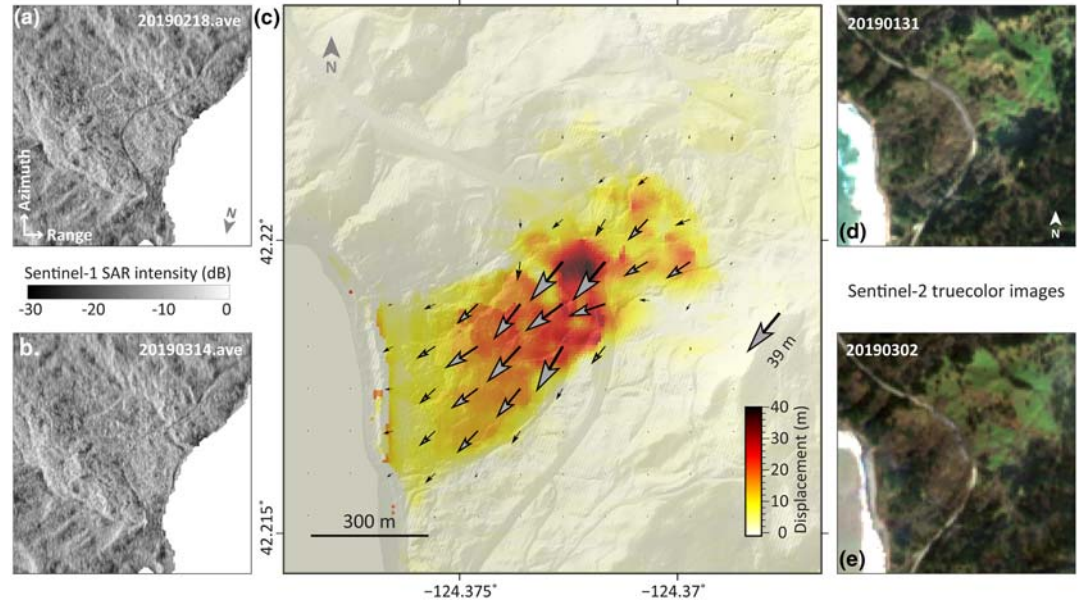


Figure 4. Three-dimensional displacement field of the February 2019 movement reconstructed from Sentinel-1/Sentinel-2 pixel offset tracking. (a and b) The averaged Sentinel-1 SAR intensity from the descending track T13 (heading angle of 194°) before and after the February 2019 slide, respectively. Both figures are shown in the radar coordinate system. The reconstructed 3-D displacement field is illustrated in (c) with arrows showing movement direction and relative magnitude. A similar map with the borehole locations added is shown in Figure S1, and the associated inversion uncertainties are depicted in Figure S2. (d and e) The two Sentinel-2 true color images used for pixel offset tracking.

$$G = \sqrt{\left(\frac{\partial H}{\partial x}\right)^2 + \left(\frac{\partial H}{\partial y}\right)^2} \quad (7)$$

where H denotes the elevation and x and y represent the easting and northing directions, respectively. The pixelwise finite difference approximations of elevation gradient for pixel $H(i, j)$ are expressed as follows:

$$G(i, j) = \sqrt{\left(\frac{H_{i+1,j} - H_{i-1,j}}{2\Delta x}\right)^2 + \left(\frac{H_{i,j+1} - H_{i,j-1}}{2\Delta y}\right)^2} \quad (8)$$

where Δx and Δy are pixel size in x and y directions, respectively. The gradient along the edges of the matrix was calculated with single-sided differences.

3.4. Reconstruction of Three-Dimensional Displacement Field

Three-dimensional displacement field of major slides can be reconstructed by combining pixel offset tracking results from both Sentinel-1A/Sentinel-1B SAR data and Sentinel-2 optical images. Defining α as the slope angle, β the slope aspect, and $\mathbf{d} = [E, N, Z]^T$ as the pixelwise displacement vector consisting of easting, northing, and upward components, respectively, \mathbf{d} is related to the measured offsets as follows:

$$\mathbf{l} \cdot \mathbf{d} = \mathbf{L} \quad (9)$$

where \mathbf{l} is the unit vector of pixel offsets in the ENZ coordinate and \mathbf{L} is the measured pixel offsets from both Sentinel-1A/Sentinel-1B and Sentinel-2 images. Equation 9 can be expanded as follows:

$$\begin{bmatrix} \cos \alpha \sin \beta & \cos \alpha \cos \beta & -\sin \alpha \\ -\cos \beta & -\sin \beta & 0 \\ 0 & 1 & 0 \\ 1 & 0 & 0 \end{bmatrix} \cdot \begin{bmatrix} E \\ N \\ Z \end{bmatrix} = \begin{bmatrix} L_{s1_AZ} \\ L_{s1_R} \\ L_{s2_N} \\ L_{s2_E} \end{bmatrix} \quad (10)$$

where L_{s1_AZ} , L_{s1_R} , L_{s2_N} , and L_{s2_E} denote offset measurements from Sentinel-1A/Sentinel-1B images in azimuth and range directions and that from Sentinel-2 images on northing and easting directions,

respectively. A weighted least squares solution was employed to solve Equation 10. Similar to Equations 3 and 4, the 3-D vector components can be obtained as $\mathbf{d} = (\mathbf{l}^T \mathbf{W} \mathbf{l})^{-1} \mathbf{l}^T \mathbf{W} \mathbf{l}$ by introducing a diagonal weight matrix \mathbf{W} based on varied accuracy of the offset measurements. The covariance matrix of \mathbf{d} can be estimated as $\mathbf{C} = (\mathbf{l}^T \mathbf{W} \mathbf{l})^{-1} \hat{\Delta}^2$, where $\hat{\Delta}^2$ is the variance of the offset tracking measurements.

Horizontal displacement vectors can be directly obtained from pixel offset tracking of two LiDAR DEMs while the vertical deformation is attainable from the elevation changes of DEM based on the measured horizontal offsets. A three-dimensional deformation field was therefore reconstructed.

4. Results

4.1. Three-Dimensional Displacement Field of the February 2019 Event

Reconstructing the three-dimensional displacement field of the major movement on 25 February 2019 was achieved by integrating pixel offset tracking of both Sentinel-1A/Sentinel-1B SAR images from descending Track T13 and Sentinel-2 images. Three-dimensional movement vectors (Figure 4c) were calculated by constructing and solving Equation 10 using the four independent observations from Sentinel-1/Sentinel-2 data. Note that each arrow in Figure 4c represents the average horizontal displacement of a 14×14 array of adjacent pixels, which corresponds to a $32\text{-m} \times 39\text{-m}$ area on the ground surface. The results show that the 2019 February major slide mainly moved along the downslope direction with an aspect of 229° (clockwise from north), though the head and toe sections have slightly larger west facing components with aspects of around 240° and 250° , respectively. The motion direction predominantly follows the regional bedding dip direction (Parker, 1979). Overall, the middle section of the slide had much larger movements than both the head and toe sections, and a maximum horizontal displacement of 39 m and a vertical movement of 13 m were observed near U.S. Highway 101 from our offset tracking results (Figure 4c). Comparison with results generated by ODOT using LiDAR DEMs acquired before and after the event demonstrates a very good mutual agreement. Two terrestrial LiDAR DEMs acquired on 16 October 2018 and 3 March 2019 revealed a maximum horizontal displacement of 40 m near the road, and both magnitude and orientation of the movement vectors match well with our results (see Britton, 2019).

4.2. Movement Rate From Airborne LiDAR DEMs

We applied pixel offset tracking to the three publicly accessible LiDAR DEMs from the Oregon Lidar Consortium (OLC, Oregon Lidar Consortium, 2020) to reveal the long-term movement rate of the Hooskanaden slide. The three freely downloadable LiDAR DEMs with a vertical RSME (root-mean-square error) of 4.6 mm were acquired on 20081017 (YYYYMMDD), 20140730, and 20160501. However, the three DEMs can only form two pairs (2008–2014 and 2008–2016) for pixel offset tracking since the 2014 and 2016 LiDAR DEMs have insufficient overlap (Figures 5a–5c).

As shown in Figure 5d, the slide section above the road had moved downslope at about 35 cm/year from 2008 to 2014, and the movement direction resembles that of the 2019 February event. Across the data-missing area below the highway, the displacement rate starts from 30 cm/year and gradually decreases toward the coast-line. A similar movement pattern was also observed from the 2008–2016 LiDAR DEM offsets (Figure 5e), and much larger motion rates of 45 cm/year were captured slightly below the road. The displacement directions remain almost identical during both the 2008–2014 and 2008–2016 periods. In contrast, the February 2019 event has much smaller south orientating components at the slide toe than the slow motions between 2008 and 2016 (Figures 4c and 5), which suggests that the 2019 major event and its slow motions might have occurred on different slip surfaces at the toe section. Various slickensides found in the borehole samples had confirmed the existence of multiple slip surfaces within the slide body (Figure 2a). Moreover, the presence of multiple slip surfaces was also indicated by the varied vertical slip angles (Figures 5f–5h), which are defined as the angles between the displacement vector and the horizontal plane:

$$\theta = \text{atan} \left(\frac{d_z}{\sqrt{d_N^2 + d_E^2}} \right) \quad (11)$$

where θ is the slip angle and d_N , d_E , and d_z are the northing, easting, and vertical displacement components, respectively. The uncertainties of estimated slip angles are within $\pm 1.2^\circ$ and $\pm 4^\circ$ for LiDAR DEMs and Sentinel-1/Sentinel-2 images, respectively, based on Equation 10.

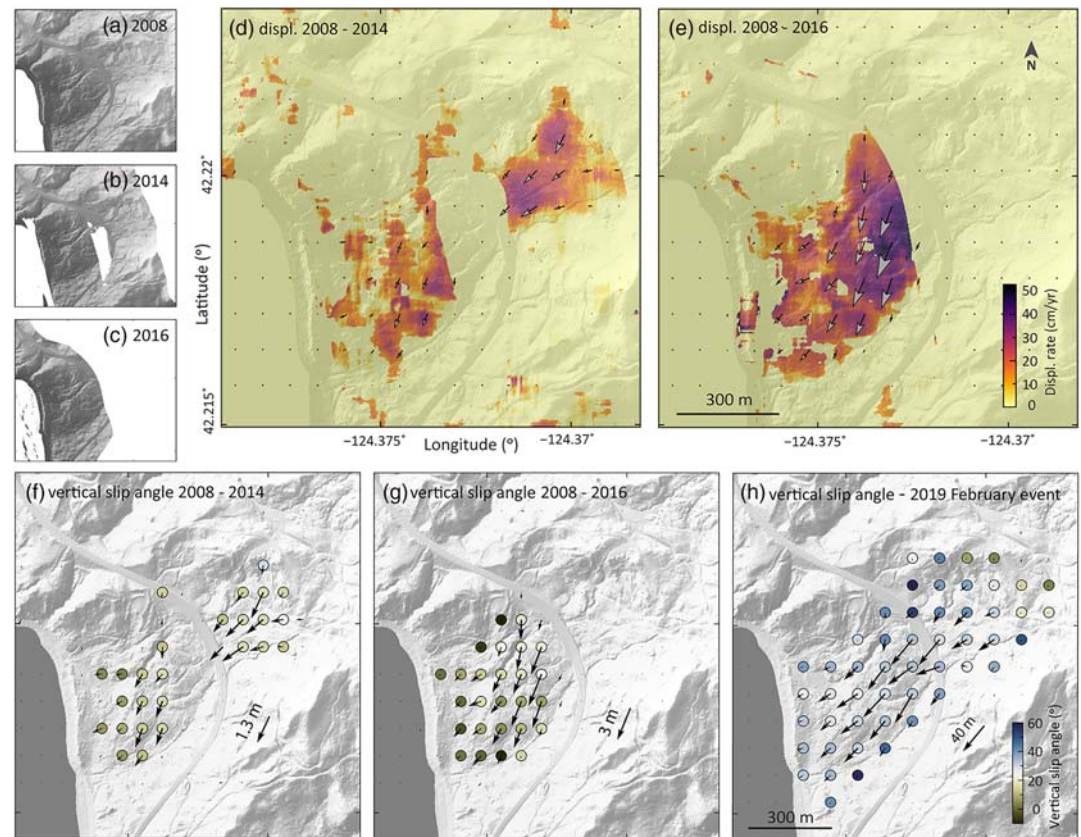


Figure 5. Cumulative slow motions of the Hooskanaden slide retrieved from LiDAR DEMs. LiDAR DEMs acquired in (a) 2008, (b) 2014, and (c) 2016 were formed into two overlapped pairs to measure displacement during (d) 2008–2014, and (e) 2008–2016, where the arrows denote direction and relative magnitude. Vertical slip angles (colored circles) of the slow movement during (f) 2008–2014, (g) 2008–2016, and (h) the February 2019 major movement, derived from the 3-D surface movement vectors. All figures cover the same spatial scope.

The inferred slip angles together suggest an overall concave-up-shaped slip surface and a rotational failure mode for the landslide, with a deepest-seated middle section near the highway (Figures 5f–5h). As is commonly seen in many landslides, the very top region of the Hooskanaden slide exhibits near-horizontal passive movements as affected by the motion of the lower section. The slip angle near the highway is $30^\circ \pm 4^\circ$, consistent with the angle of 31.4° inferred from ODOT’s report (ODOT, Oregon Department of Transportation, 2019).

4.3. Motion Dynamics From 2007 to 2019

To reveal historical motion behaviors of the slide, 21 ALOS images from ascending Track T224 between February 2007 and January 2011, and 84 Sentinel-1A/Sentinel-1B images from ascending Track T35 between July 2016 and October 2019 were processed with InSAR to retrieve the movement time series from 2007 to 2019. The gap between 2011 and 2016 was bridged with tracked pixel offsets from LiDAR DEMs (Figure 6a). InSAR measurements separated by the 2016 and 2019 events were bridged together by using averaged motion rates right before and after the events (Figure 6a), as the large event displacements caused jumps of InSAR phase by over 2π and therefore cannot be directly measured by the InSAR method (Rosen et al., 2000; Xu et al., 2019). The 2008–2016 LiDAR DEM offsets do not cover the upper half of the landslide. A reference area below the road (blue dashed box in Figure 6b) was selected to infer the 2008–2016 motion rates above the road based on the averaged displacement rate from ALOS observations (Figure 6b).

As seen from Figures 6a and 7, the long-term slow motion exhibits seasonal variations. Annually, most displacements took place during the wet winter seasons along with faster movement rates, whereas little deformation occurred during the dry summer seasons. The starting dates of the winter acceleration vary by years (e.g., approximately 27 October 2016, 27 November 2017, 13 December 2018, and 6 October 2019) but have

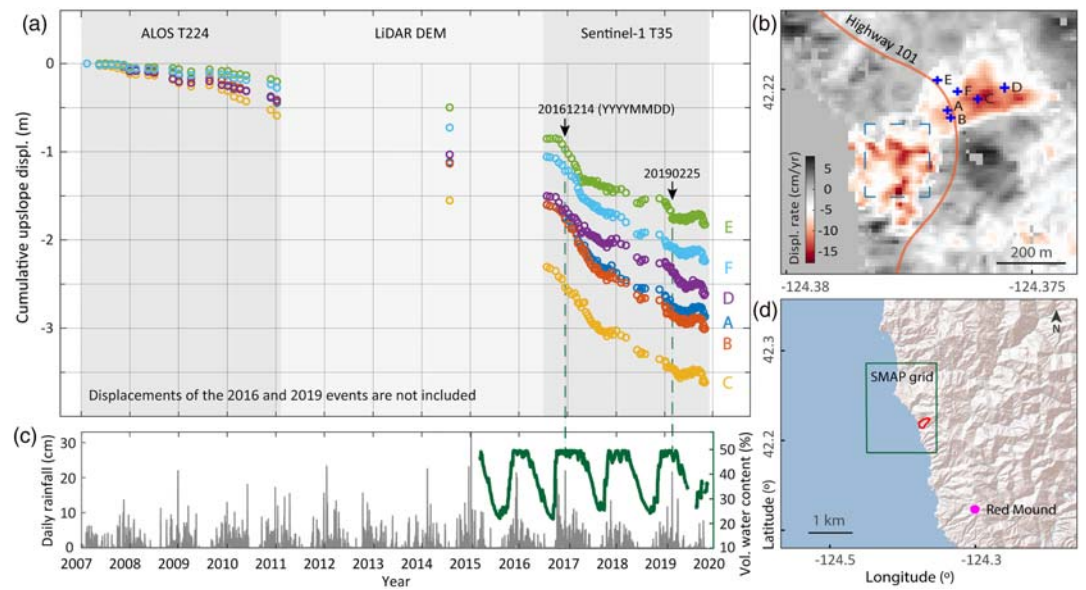


Figure 6. Long-term motion dynamics of the Hooskanaden slide from 2007 to 2019. (a) Cumulative along-slope displacements of Points A–F as shown in (b) retrieved from ALOS, LiDAR DEM and Sentinel-1A/Sentinel-1B data. Note that along-slope displacements of the 2016 event (~4 m) and the 2019 event (~43 m) are not included for figure clarity. Average coherences of the used interferograms are depicted in Figure S3. (b) Average along-slope movement rate from 2007–2011 ALOS InSAR. The dashed rectangle denotes the reference area used for helping interpret offsets from LiDAR DEMs. (c) Daily precipitation (gray bars) and root zone SMAP soil moisture (green polyline) from a 12-km-distant meteorological station (red mound) and a 9×9-km SMAP grid respectively as shown in (d). Note that SMAP soil moisture is shown in volumetric water content rather than effective saturation level.

good correspondence to the root zone SMAP soil moisture (average value of the top ~1-m depth) that reveals soil saturation level (Figure 6c): wet-season acceleration usually starts 3–5 weeks after the wet season arrives (defined as 25% postsummer soil moisture rise) (Figures 6a and 6c and 7a and 7c; Xu et al., 2019). Essentially, the rapid postsummer rise and a constant winter-season high level of soil moisture implies a nearly continuous input of water infiltration after the onset of wet seasons, which would gradually infiltrate downward to elevate basal pore pressure and trigger/accelerate slide motion by reducing effective normal stress and consequent frictional shear resistance along the landslide base (Terzaghi, 1950).

The decadal-scale slow motion of the slide presents an overall accelerating trend, with an average downslope rate of 13 cm/year from 2007–2011, 21 cm/year from 2011 to 2016, and 53 cm/year from 2016 to 2019 (Figure 6a). The long-term accelerating trend could be attributed to coastal erosion of the landslide toe (see Discussion). Both the 2016 moderate movement and the 2019 major movement occurred in the wet season while SMAP soil moisture remained at a constant high level of around 49%. However, the 2006 event happened 68 days after the wet season started, while the 2019 event took place after 92 days into the wet season (Figure 6c). These variable lag times illustrate that shallow soil moisture may be indicative of general, overall groundwater conditions, but may not directly reveal the movement behavior of deep landslides. In fact, the exceptionally heavy rainfall in December 2016 and February 2019 suggests that the moderate/major slide events were likely triggered by short-term but high-intensity rainfall spikes (Figures 6a, 6c, and 7).

Figures 6 and 7 show that postevent movement rates of the points (A–F) remain almost unchanged from those before the 2016 and 2019 moderate/major events. The water year 2017 (1 September 2016 to 1 September 2017) experienced the longest wet season and the greatest cumulative rainfall compared to water years 2018 and 2019, as indicated by soil moisture and water-year rainfall records (Figure 7c). Water year 2017 is also the water year that the landslide had the greatest annual displacements and nonstop movements even during summer (Figures 6a and 7a). In contrast, all six points (A–F) had lower total displacements in both water years 2018 and 2019 and had temporary movement stoppages in both 2018 and 2019 summers. All the above observations indicate a strong correlation between precipitation and the landslide's slow motions.

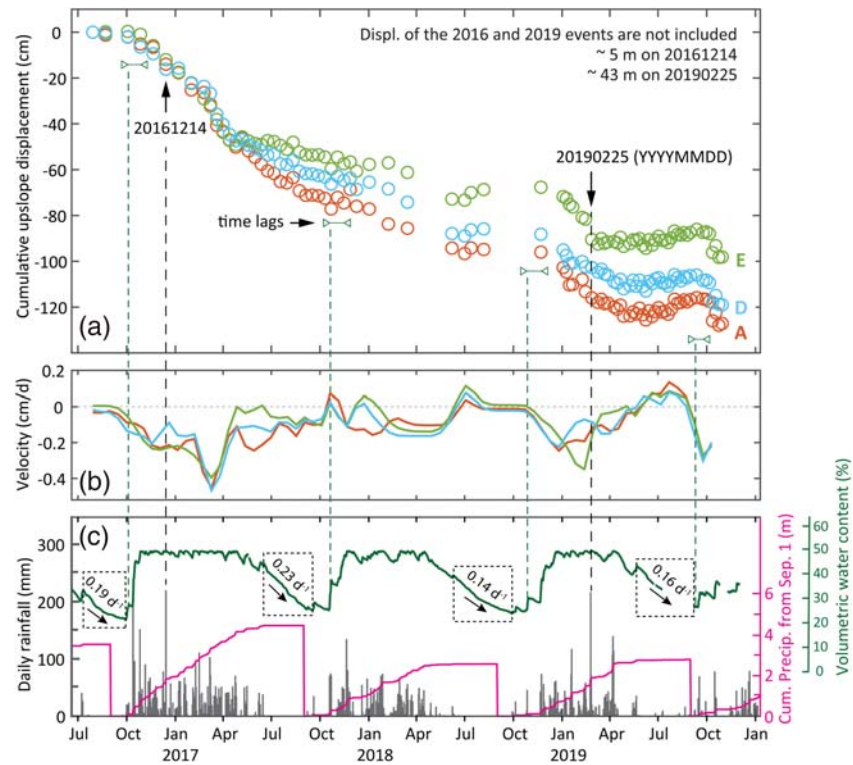


Figure 7. A closeup of the landslide motion dynamics between 2016 and 2019. (a) Cumulative along-slope displacements of three points (A, D, and E as shown in Figure 6b), and time lags between arrival of wet seasons and seasonal accelerations from 2016 to 2019. (b) Movement rates of the three points (in consistent colors) obtained from displacement time series using forward difference approximations. (c) Daily rainfall (gray bars), cumulative water-year rainfall starting from 1 September (red line), and soil moisture (green line) are scaled by y axes in corresponding colors. The dashed boxes show drop rates of soil moisture during dry summers.

4.4. Estimation of Hydraulic Conductivity and Diffusivity

Borehole inclinometer measurements from a borehole slightly below the highway (BH-5 in Figure 2) between 1 December 2017 and the end of January 2018 reveal that the slow block-like motion of the slide during this period dominantly occurred on a 33-m-deep basal surface. Very slight displacements had also taken place on two potential slip surfaces at ~15- and ~21-m level below the ground surface (Alberti et al., 2020; Castro et al., 2019). The groundwater level was found 3 m beneath the surface during drilling in December 2017 (Figure 2a). Assuming that the postsummer precipitation vertically infiltrates into soils as a convective flow above the groundwater table and transmits elevated pore pressure to the basal surface in an approximately diffusive manner below the groundwater table and that landslide acceleration temporally correlates with elevation of basal pore pressure, the characteristic hydraulic conductivity and diffusivity at the borehole can be estimated based on the time lags between rainfall pulse and InSAR captured slide acceleration (Xu et al., 2019).

For the unsaturated soils above the groundwater level during dry summers, the unsaturated hydraulic conductivity K relates to the saturated hydraulic conductivity K_s as (Van Genuchten, 1980):

$$K = K_s S_e^L \left\{ 1 - [1 - S_e^{\frac{n}{n-1}}]^{1 - \frac{1}{n}} \right\}^2 \quad (12)$$

where the effective saturation $S_e = \frac{\theta - \theta_r}{\theta_s - \theta_r}$ is related to measured volumetric water content θ , residual water content θ_r , and saturated water content θ_s (Brooks & Corey, 1964; Rawls et al., 1982). $L = 0.5$ is an empirical parameter and $n = 2$ is a measure of pore size distribution (Mualem, 1976; Schaap et al., 2001). The time lag, T_k , for the advective flow to infiltrate downward by h_k can be estimated as $T_k = h_k/K$. In the

saturated soils, the pore pressure response can be approximated as one-dimensional transmission and attenuation of rainfall-induced oscillating flux from the top surface (i.e., the groundwater table for the partially drained summer soils or the ground surface for the fully saturated wet-season soils):

$$\frac{\partial P}{\partial t} = D_0 \frac{\partial^2 P}{\partial z^2} \quad (13)$$

where P is pore water pressure head, t is time, D_0 is hydraulic diffusivity, and z is depth. The time lag, T_d , between the sinusoidally oscillating source signal and the pressure peak response at depth h_d can be solved as (Baum & Reid, 1995; Carslaw & Jaeger, 1959)

$$T_d = h_d \sqrt{\frac{t_0}{4\pi D_0}} \quad (14)$$

where t_0 is the period of the oscillating signal, and here t_0 was assumed as 1 day based on rainfall records. An empirical relationship between the magnitude of saturated hydraulic conductivity K_s and hydraulic diffusivity D_0 is that $D_0/K_s = dP/d\theta = 10^2$ (in consistent length and time units) (Mualem, 1976; Van Genuchten, 1980). The time lags, $T = T_k + T_d$, between the arrival of the wet season (defined by a 25% postsummer soil moisture rise) and postsummer slide acceleration were observed ranging from 16 to 37 days in years 2016, 2017, 2018, and 2019 (Figure 7a). Taking 49% as the saturated water content and 28% as the measured unsaturated water content of the surface-1-m soils (Figure 7c), the averaged characteristic hydraulic conductivity K_s and diffusivity D_0 were estimated as 6.6×10^{-6} m/s and 6.6×10^{-4} m²/s, respectively.

5. Discussion

5.1. Enhancement of Pixel Offset Tracking

Pixel offset tracking is one of the key methods used for this investigation to measure slide displacements. Stacking multiple Sentinel-1 SAR images and combining multiple bands of Sentinel-2 acquisitions are of significant importance to highlight the ground feature and enhance offset tracking performance. For Sentinel-2 data, integrating information from multiple bands could potentially improve offset tracking performance. For LiDAR DEMs, elevation gradients are more reliable ground features for block-like landslides than the elevation itself, but neither one would work for debris flows that have entirely altered the original topography. In addition to the elevation gradient (Equation 7), the second-order gradient G_2 could be a useful alternative for highlighting ground features from DEMs:

$$G_2 = \sqrt{\left(\frac{\partial^2 H}{\partial x^2}\right)^2 + \left(\frac{\partial^2 H}{\partial y^2}\right)^2} \quad (15)$$

where H is the elevation and x and y denote the easting and northing directions, respectively. However, our tests on the 2008, 2014, and 2016 LiDAR DEMs show that second-order gradient may also magnify noises and contaminate the results. Therefore, G_2 should be used with caution.

5.2. Proposed Rainfall Threshold for the Moderate/Major Events

Figures 6 and 7 show that movements of the Hooskanaden landslide are predominantly associated with precipitation. To further understand the hydrological settings that bifurcate the sliding behavior into slow motions and moderate/major events, 25-year daily precipitation from the Red Mound station (Figure 6d) between 1994 and 2020 and hourly precipitation near the historical moderate/major events were collected and processed. As shown in Figure 8a, the four moderate/major movements in 1995, 2006, 2016, and 2019 occurred neither on dates with maximum cumulative water-year rainfall (starting from 1 September), nor on the date with the most intense daily rainfall over the 25 years (i.e., 6 January 2015). Moreover, thresholding previous 3-day and previous 15-day cumulative rainfall would also fail to predict the dates of the moderate/major events without generating numerous false alarms (Figures 8b and 8c).

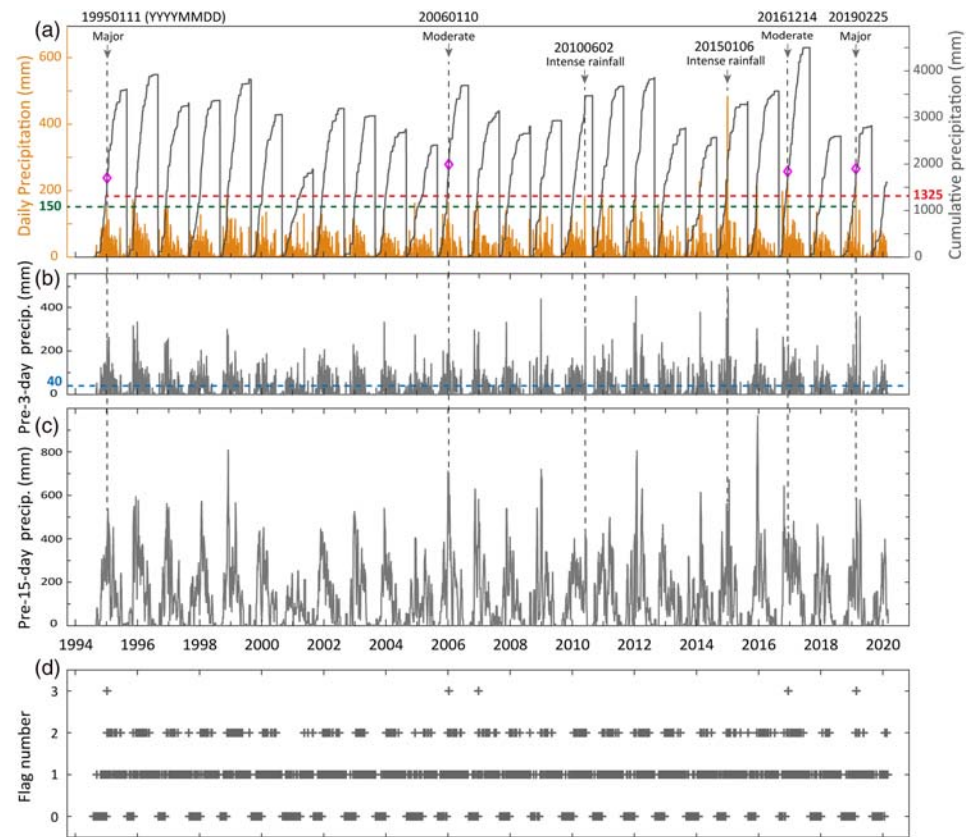


Figure 8. Rainfall thresholds for forecasting moderate/major landslide events. (a) Daily precipitation (brown bars), cumulative precipitation starting from every 1 September (gray lines), and moderate and major events (magenta diamonds). (b) Previous 3-day and (c) previous 15-day cumulative precipitation. Our proposed threefold rainfall threshold comprises antecedent water-year cumulative rainfall (red dashed lines in a), daily rainfall (green dashed lines in a), and previous 3-day precipitation (blue dashed line in b). A close-up of previous 3-day rainfall threshold is shown in Figure 9a with a red dashed line. (d) The flag number denotes how many components of the three-component threshold were met on a specific day between 1994 and 2020.

Here, we propose a threefold threshold composed of three components of different time scales to better predict the moderate/major events of the Hooskanaden landslide: 150-mm daily rainfall, with previous 3-day cumulative rainfall of 40 mm and antecedent water-year precipitation of 1,325 mm after 1 September. Essentially, the water-year-scale antecedent precipitation is used as a proxy for soil saturation level (nearly continuous infiltration of 1,325-mm rainfall would fully saturate the landslide depth after a dry summer), and a daily-scale intense rainfall allows generation of a strong pore pressure pulse to trigger a moderate/major landslide. The 3-day-scale antecedent rainfall ensures that the top soil layers are moist enough to allow generation of a strong pore pressure pulse by an intense daily rainfall.

The proposed threefold threshold can accurately predict the dates for the four moderate/major events between 1995 and 2020 with only one false alarm on 20061215 [YYYYMMDD] (Figures 8a, 8d, and 9a). Worth mentioning is that the 3-day-scale rainfall threshold of 40 mm successfully eliminated two potential false alarms on dates with over 150 mm daily rainfall (i.e., 20100602 and 20150106). A detailed look of the daily and hourly rainfall records reveals that the intense precipitation on 20100602 occurred after seven consecutive dry days, and the extremely intense precipitation on 20150106 (481.58 mm of rainfall fell within 1 hr) also occurred after 12 continuously dry days (Figures 9c and 9d). The real pore pressure pulse caused by the storms could have been significantly reduced by what might be expected due to rainwater absorption within the upper, drier part of the landslide and due to overland flows (rainfall rate exceeds K), and consequently was not able to trigger a moderate/major movement. Using the averaged drop rate of soil moisture during summers (see black dashed boxes in Figure 7c), we estimated that soil moisture would drop from 0.49

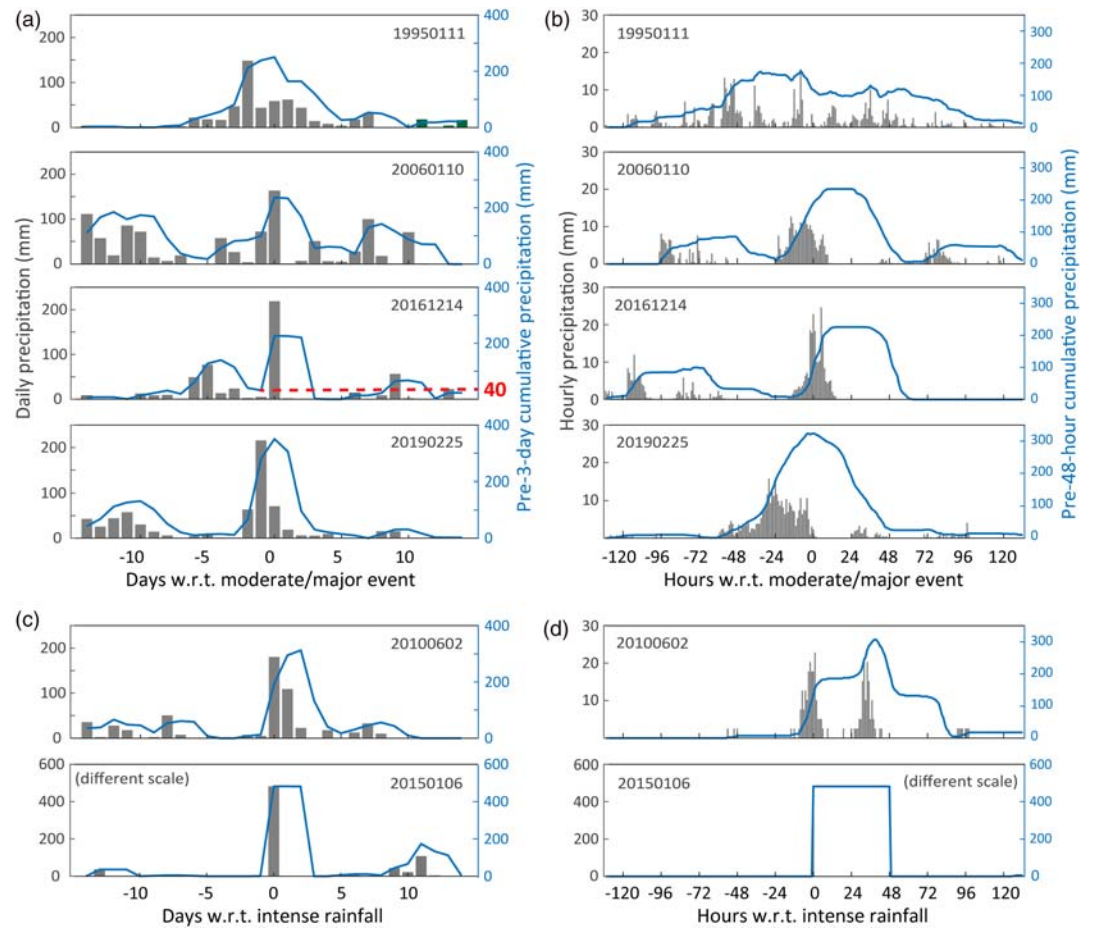


Figure 9. Daily and hourly precipitation near special dates. (a) Daily and (b) hourly rainfall near the moderate and major landslide events, where negative x axis values represent days/hours before the event. (c) Daily and (d) hourly rainfall for two special dates when intense rainfall did not trigger larger landslide movement. Blue lines in (a) and (c) represent previous 3-day cumulative rainfall, while those in (b) and (d) denote previous 48-hr cumulative precipitation. The red dashed line in (a) marks the minimum previous 3-day cumulative precipitation in our proposed threefold rainfall threshold.

to 0.484 after three consecutive dry days, and the corresponding unsaturated hydraulic conductivity K would drop by 30% from 6.6×10^{-6} to 4.64×10^{-6} m/s (Figure 10c) based on Equation 12. An empirical 40-mm threshold of previous 3-day cumulative rainfall was therefore set to avoid false alarms caused by dried upper soil layers, based on historical preceding 3-day rainfall records (Figures 9a and 9c).

The threshold of the antecedent water-year rainfall is tied to the antecedent groundwater level and summer soil moisture. Borehole drilling on 1 December 2017 revealed a groundwater level 3 m below the surface at the Hooskanaden landslide (Figure 2a). Daily logs of a groundwater well (CURR 819) 23.5 km southeast of the landslide show that groundwater levels increased from 16.1 m above sea level (water-year low) on 1 September 2017 to 18.4 m (water-year peak) on 9 April 2018 at the site. The threshold implies a lower bound of groundwater level of -5.3 m at the landslide site in 2017 summer, and consequently an $\sim 1,325$ -mm cumulative precipitation to fully saturate the landslide materials, as SMAP data show that average soil moisture of the top 1-m soils shows a minimum of 25% during the 2017 summer (Figure 7c). The daily rainfall threshold was set empirically based on daily rainfall records of the first moderate/major event (the 1995 one) shown in Figure 8a and can yield accurate forecasting, as validated by the other three later events in 2006, 2016, and 2019. Note that the moderate/major slides may have been triggered by an extremely short-term rainfall spike in a rainy day, which may require rainfall records with finer time scale such as every 5 min to be better understood.

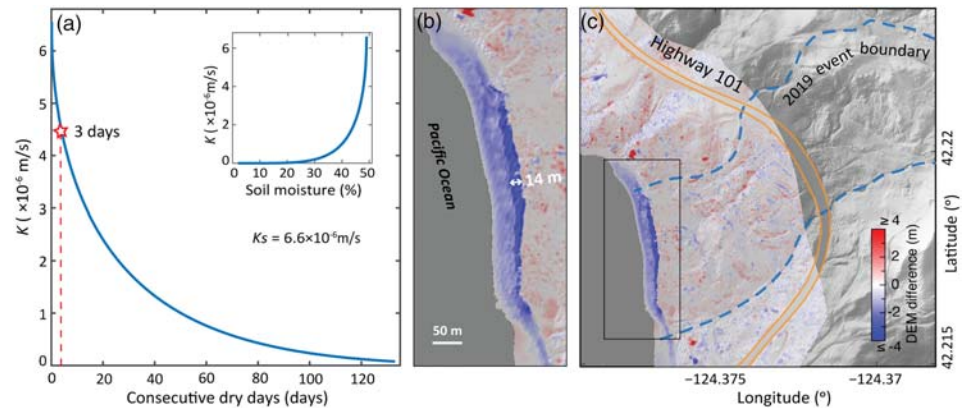


Figure 10. Unsaturated hydraulic conductivity and coastal erosion. (a) Changes of unsaturated hydraulic conductivity K_s with regard to consecutive drying days and soil moisture. (b) Elevation differences between the 2016 and 2008 LiDAR DEMs at the landslide toe, which is enlarged from the black box in (c).

Determining the proposed threefold rainfall threshold requires precipitation time series, landslide thickness and groundwater depth, hydraulic parameters of the landslide material, and past landslide motion records (or soil mechanical parameters). These data and parameters can be obtained through variable means depending on the specific case. Here for the Hooskanaden landslide we employed primarily remote sensing data and ground-based hydrological observations, and our methods can be easily adapted for other similar landslides globally to serve for landslide movement forecasting. Overall, the concept of the “three-component” threshold that accounts for various hydrological processes could be applicable to many deep-seated landslides, but the exact threshold for each component must be site specific and could be derived from field observations and/or empirical values.

5.3. Mechanism of Landslide Motions Modulated by Precipitation and Coastal Erosion

Overall, our analysis has confirmed that both slow motions and moderate/major events of the Hooskanaden landslide are controlled by precipitation, though the exact processes differ. The slow motion usually starts 3–5 weeks after the wet season arrives (defined by a 25% postsummer soil moisture rise) and is controlled by both rainwater infiltration of the top dry layers (unsaturated during summer) and pore pressure transmission in saturated soils (Figures 6a and 7a; Xu et al., 2019). In contrast, moderate/major slide events respond much faster to rainfall pulses, for example, in approximately 2 days, as the soils are almost saturated in the midst of a wet season and the slide has already been moving (Figure 9). Consequently, both rainfall loading and pulses of increased pore pressure can quickly accelerate the existing slow motion into a moderate/major slide event. The slowdown of sliding movement can be primarily attributed to pore pressure drop due to decreased rainfall input and subsurface drainage. In addition, Figures 9a and 9b reveal that time lags between the daily rainfall pulse and the slide accelerations range from 1–2 days, which matches very well with our hydraulic diffusivity estimation of 6.6×10^{-4} m²/s and the landslide’s observed depth. To illustrate, pore pressure diffusion for $H = 33$ m roughly takes $T_d = 1.23$ days, as calculated using the estimated hydraulic diffusivity and Equation 14.

Our remote sensing observations revealed an accelerating trend of the landslide movements from 2007 to 2019 (Figure 6a), which could be attributed to coastal erosion of the landslide toe. Elevation differencing of the 2016 and 2008 LiDAR DEMs demonstrates that the landslide toe has undergone significant erosion from 2009 to 2016: ~14 m wide of the coast has elevation drops of over 4 m. The annual coastline retreat rate at the landslide toe is ~1.9 m/year, which might have led to the long-term acceleration of landslide motions by reducing passive resistance.

6. Conclusions

Multiple remote sensing data sets and processing methods, borehole measurements, and hydrological observations have been used in this investigation to understand 12-year motion dynamics of the Hooskanaden landslide that exhibited both long-term slow movements and short-term moderate/major slide events.

Pixel offset tracking of both Sentinel-1 SAR images and Sentinel-2 optical images was carried out to reconstruct the three-dimensional displacement field of the 2019 February major movement. Offsets of LiDAR DEMs were obtained by using elevation gradients to reveal the 3-D motion rates of the landslide between 2008 and 2016. Together with InSAR processing of ALOS and Sentinel-1 SAR images, a 12-year displacement history of the Hooskanaden landslide has been retrieved.

Movement rates of the landslide exhibit substantial seasonal variations on an annual scale with dominating wet-season displacements, and an overall accelerating trend can be seen over the past decade potentially due to coastal erosion. Pixel offset tracking was successfully applied to the Sentinel-1/Sentinel-2 images and LiDAR DEMs to recover the three-dimensional displacement field of the 2019 February major movement, and to reveal that the rapid movement and slow motions may have occurred on slightly different slip surfaces. By using satellite captured SMAP soil moisture and InSAR derived time lags for postsummer rainfall to trigger the first seasonal sliding acceleration, the averaged characteristic hydraulic conductivity K_s and diffusivity D_0 of the landslide materials were estimated as 6.6×10^{-6} m/s and 6.6×10^{-4} m²/s, respectively. These produce timing estimations that agree with the observed 2-day time lag for rainfall pulses to trigger the 1995, 2006, 2016, and 2019 moderate/major movements. Comparison between the motion history and ground rainfall records demonstrates that thresholding pre-3-day and pre-15-day cumulative precipitation cannot lead to effective prediction of dates for moderate/major events. In contrast, more accurate prediction can be achieved by using our proposed threefold threshold of 150-mm daily rainfall, with previous 3-day cumulative rainfall of 40 mm and antecedent water-year precipitation of 1,325 mm after 1 September.

Our study demonstrates the utility of integrating multiple remote sensing methods (InSAR and pixel offset tracking) and data sets (ALOS and Sentinel-1 SAR, Sentinel-2 optical images, and LiDAR DEMs) to retrieve long-term displacement time series and achieve 3-D characterizations of a landslide, which are of great significance for forecasting the landslide's future motions (e.g., seasonal accelerations and decelerations, the rotation failure mode, and the long-term acceleration associated with coastal erosion). Furthermore, we propose a new threefold rainfall threshold based on shallow soil moisture from SMAP and 15-year ground precipitation records to forecast both the seasonal onset of creeping motion as well as moderate/major events of the Hooskanaden landslide. The ability of the proposed threshold has been explained with hydrological modeling and remote sensing observations. Our approaches for developing the threshold predominantly rely on remote sensing data and ground precipitation and do not require expensive and labor-intensive pore pressure monitoring and therefore can be easily adapted for similar landslides worldwide.

Data Availability Statement

ALOS PALSAR data sets were copyrighted by the Japan Aerospace Exploration Agency (JAXA) and provided by Alaska Satellite Facility (ASF). Copernicus Sentinel data 2016–2019 processed by European Space Agency (ESA) were retrieved from ASF Distributed Active Archive Center (DAAC). SMAP soil moisture data were provided by the National Aeronautics and Space Administration (NASA). LiDAR DEMs were accessed from Oregon Lidar Consortium. Data that support this study are available online (at <https://smu.box.com/v/HooskanadenSlide>).

Acknowledgments

This study benefited from the support provided by Jill DeKoekkoek, Dan Latham, Ben Leshchinsky, Pete Castro, Audrey Britton, and Tidewater Contractors, Inc. This research was financially supported by NASA Interdisciplinary Research (IDS) in Earth Science Program (80NSSC17K0022) and the Shuler-Foscoe Endowment at Southern Methodist University. We thank Jonathan Perkins, Estelle Chaussard, Noah Finnegan, and one anonymous reviewer for providing suggestions that improved this manuscript. Any use of trade, firm, or product names is for descriptive purposes only and does not imply endorsement by the U.S. government.

References

- Alberti, S., Senogles, A., Kingen, K., Booth, A., Castro, P., DeKoekkoek, J., et al. (2020). The Hooskanaden landslide: Historic and recent surge behavior of an active earthflow on the Oregon Coast. *Landslides*, 1–14.
- Angeli, M. G., Gasparetto, P., Menotti, R. M., Pasuto, A., & Silvano, S. (1996). A visco-plastic model for slope analysis applied to a mudslide in Cortina d'Ampezzo, Italy. *Quarterly Journal of Engineering Geology and Hydrogeology*, 29(3), 233–240. <https://doi.org/10.1144/GSL.QJEGH.1996.029.P3.06>
- Bamler, R., & Eineder, M. (2005). Accuracy of differential shift estimation by correlation and split-bandwidth interferometry for wideband and delta-k SAR systems. *IEEE Geoscience and Remote Sensing Letters*, 2(2), 151–155. <https://doi.org/10.1109/LGRS.2004.843203>
- Baum, R. L., & Reid, M. E. (1995). Geology, hydrology, and mechanics of a slow-moving. In *Clay and shale slope instability* (Vol. 10, p. 79). Boulder, CO: The Geological Society of America, Inc. <https://doi.org/10.1130/REG10-p79>
- Bernstein, R., & Colby, C. (1983). Image geometry and rectification. *Manual of remote sensing*, 1, 873–922.
- Britton, M. A. (2019). *Study of the Hooskanaden slide using LiDAR technology*. Paper presented at 2019 Symposium by the Sea. Retrieved from <https://www.orurisa.org/resources/Audrey%20McHugh-Britton%20OregonDOT%20Hooskanaden%20Slide.pdf>
- Brooks, R. H., & Corey, A. T. (1964). *Hydraulic properties of porous media*, Hydrology Paper (Vol. 3). Fort Collins: Colorado State University.
- Carlsaw, H. S., & Jaeger, J. C. (1959). *Conduction of heat in solids*. Oxford: Clarendon Press.
- Castro, P., Mohny, C., DeKoekkoek, J., & Cunningham, C. (2019). Hooskanaden landslide reconnaissance in response to 2019 episodic movement; Oregon Coast Hwy (US 101) (Hwy. 9, M.P. 343.5), Curry County, Oregon.

- Entekhabi, D., Yueh, S., & De Lannoy, G. (2014). SMAP handbook.
- Froude, M. J., & Petley, D. (2018). Global fatal landslide occurrence from 2004 to 2016. *Natural Hazards and Earth System Sciences*, 18(8), 2161–2181. <https://doi.org/10.5194/nhess-18-2161-2018>
- Gasparetto, P., Mosselman, M., & Van Asch, T. W. (1996). The mobility of the Alvera landslide (Cortina d'Ampezzo, Italy). *Geomorphology*, 15(3–4), 327–335. [https://doi.org/10.1016/0169-555X\(95\)00078-J](https://doi.org/10.1016/0169-555X(95)00078-J)
- Lu, Z., & Dzurisin, D. (2014). *InSAR imaging of Aleutian volcanoes: Monitoring a volcanic arc from space*. Berlin/Heidelberg, Germany: Springer. <https://doi.org/10.1007/978-3-642-00348-6>
- Mackey, B. H., & Roering, J. J. (2011). Sediment yield, spatial characteristics, and the long-term evolution of active earthflows determined from airborne LiDAR and historical aerial photographs, Eel River, California. *Bulletin*, 123(7–8), 1560–1576. <https://doi.org/10.1130/B30306.1>
- Massey, C. I., Petley, D. N., & McSaveney, M. J. (2013). Patterns of movement in reactivated landslides. *Engineering Geology*, 159, 1–19. <https://doi.org/10.1016/j.enggeo.2013.03.011>
- Mualem, Y. (1976). A new model for predicting the hydraulic conductivity of unsaturated porous media. *Water Resources Research*, 12(3), 513–522. <https://doi.org/10.1029/WR012i003p00513>
- ODOT (Oregon Department of Transportation) (2019). Hooskanaden slide update. Retrieved from http://www.co.curry.or.us/2019_05_%20Hooskanaden%20Slide%20Update%20ODOT.pdf
- OLC (Oregon Lidar Consortium) (2020). LiDAR data viewer. <https://gis.dogami.oregon.gov/maps/lidarviewer/>
- Ollinger, S. V. (2011). Sources of variability in canopy reflectance and the convergent properties of plants. *New Phytologist*, 189(2), 375–394. <https://doi.org/10.1111/j.1469-8137.2010.03536.x>
- Orr, E. L., & Orr, W. N. (2012). *Oregon geology* (6th ed.). Corvallis: Oregon State University Press.
- Parker, E. (1979). Progress report—Hooskanaden Creek slide drilling, Oregon Coast Highway/Curry County.
- Pyles, M. R., Mills, K., & Saunders, G. (1987). Mechanics and stability of the Lookout Creek earth flow. *Bulletin of the Association of Engineering Geologists*, xxiv(2), 267–280. <https://doi.org/10.2113/gsegeosci.xxiv.2.267>
- Rawls, W. J., Brakensiek, D. L., & Saxton, K. E. (1982). Estimation of soil water properties. *Transactions of ASAE*, 25(5), 1316–1320. <https://doi.org/10.13031/2013.33720>
- Rodriguez, E., & Martin, J. M. (1992). Theory and design of interferometric synthetic aperture radars. *IEEE Proceedings F (Radar and Signal Processing)*, 139(2), 147–159. <https://doi.org/10.1049/ip-f-2.1992.0018>
- Rosen, P. A., Hensley, S., Joughin, I. R., Li, F. K., Madsen, S. N., Rodriguez, E., & Goldstein, R. M. (2000). Synthetic aperture radar interferometry. *Proceedings of the IEEE*, 88(3), 333–382. <https://doi.org/10.1109/5.838084>
- Scambos, T. A., Dutkiewicz, M. J., Wilson, J. C., & Bindshadler, R. A. (1992). Application of image cross-correlation to the measurement of glacier velocity using satellite image data. *Remote Sensing of Environment*, 42(3), 177–186. [https://doi.org/10.1016/0034-4257\(92\)90101-O](https://doi.org/10.1016/0034-4257(92)90101-O)
- Schaap, M. G., Leij, F. J., & van Genuchten, M. T. (2001). Rosetta: A computer program for estimating soil hydraulic parameters with hierarchical pedotransfer functions. *Journal of Hydrology*, 251(3–4), 163–176. [https://doi.org/10.1016/S0022-1694\(01\)00466-8](https://doi.org/10.1016/S0022-1694(01)00466-8)
- Schulz, W. H., McKenna, J. P., Kibler, J. D., & Biavati, G. (2009). Relations between hydrology and velocity of a continuously moving landslide—Evidence of pore-pressure feedback regulating landslide motion? *Landslides*, 6(3), 181–190. <https://doi.org/10.1007/s10346-009-0157-4>
- Schulz, W. H., Smith, J. B., Wang, G., Jiang, Y., & Roering, J. J. (2018). Clayey landslide initiation and acceleration strongly modulated by soil swelling. *Geophysical Research Letters*, 45, 1888–1896. <https://doi.org/10.1002/2017GL076807>
- Simoni, A., Ponza, A., Picotti, V., Berti, M., & Dinelli, E. (2013). Earthflow sediment production and Holocene sediment record in a large Apennine catchment. *Geomorphology*, 188, 42–53. <https://doi.org/10.1016/j.geomorph.2012.12.006>
- Spiker, E. C., & Gori, P. (2003). National landslide hazards mitigation strategy, a framework for loss reduction (No. 1244). US Geological Survey. <https://doi.org/10.3133/cir1244>
- Tarantola, A. (2005). Inverse problem theory and methods for model parameter estimation (Vol. 89). SIAM. <https://doi.org/10.1137/1.9780898717921>
- Terzaghi, K. (1950). Mechanism of landslides. In *Application of geology to engineering practice* (Ch. 5, pp. 202–245). New York: The Geological Society of America. <https://doi.org/10.1130/Berkey.1950.83>
- Tong, X., & Schmidt, D. (2016). Active movement of the Cascade landslide complex in Washington from a coherence-based InSAR time series method. *Remote Sensing of Environment*, 186, 405–415. <https://doi.org/10.1016/j.rse.2016.09.008>
- Van Genuchten, M. T. (1980). A closed-form equation for predicting the hydraulic conductivity of unsaturated soils. *Soil Science Society of America Journal*, 44(5), 892–898. <https://doi.org/10.2136/sssaj1980.03615995004400050002x>
- Walker, G. W., & MacLeod, N. S. (1991). Geologic map of Oregon. U.S. Geological Survey. Map Scale: 1:500,000
- Werner, C., Wegmüller, U., Strozzi, T., & Wiesmann, A. (2000, October). *Gamma SAR and interferometric processing software* (Vol. 1620, p. 1620). Paper presented at Proceedings of the ERS-Envisat Symposium, Gothenburg, Sweden.
- WRCC (Western Regional Climate Center) (2020). Remote automatic weather stations. <https://wrcc.dri.edu>
- Xu, Y., Kim, J., George, D. L., & Lu, Z. (2019). Characterizing seasonally rainfall-driven movement of a translational landslide using SAR imagery and SMAP soil moisture. *Remote Sensing*, 11(20), 2347. <https://doi.org/10.3390/rs11202347>